Original Article

Institution of MECHANICAL ENGINEERS

Journal of MECHANICAL ENGINEERING SCIENCE

Proc IMechE Part C:
J Mechanical Engineering Science
0(0) 1–14

DOI: 10.1177/0954406220967687
journals.sagepub.com/home/pic
SAGE

Tail shapes lead to different propulsive mechanisms in the body/caudal fin undulation of fish

Jialei Song[1], Yong Zhong[2], Ruxu Du[2], Ling Yin[1] and Yang Ding[3]

Abstract

In this paper, we investigate the hydrodynamics of swimmers with three caudal fins: a round one corresponding to snakehead fish (*Channidae*), an indented one corresponding to saithe (*Pollachius virens*), and a lunate one corresponding to tuna (*Thunnus thynnus*). A direct numerical simulation (DNS) approach with a self-propelled fish model was adopted. The simulation results show that the caudal fin transitions from a pushing/suction combined propulsive mechanism to a suction-dominated propulsive mechanism with increasing aspect ratio (*AR*). Interestingly, different from a previous finding that suction-based propulsion leads to high efficiency in animal swimming, this study shows that the utilization of suction-based propulsion by a high-*AR* caudal fin reduces swimming efficiency. Therefore, the suction-based propulsive mechanism does not necessarily lead to high efficiency, while other factors might play a role. Further analysis shows that the large lateral momentum transferred to the flow due to the high depth of the high-*AR* caudal fin leads to the lowest efficiency despite the most significant suction.

Keywords

Fish swimming, undulatory locomotion, caudal fin shape, suction-based propulsion

Date received: 18 May 2020; accepted: 17 September 2020

Introduction

The geometry of the fish caudal fin exhibits a wide range of diversities, varying from concave to convex on the trailing edge. It is usually associated with a suitable undulation mode: fish using the anguilliform mode have the caudal fin with a low aspect ratio, while those using the thunniform mode have the caudal fin with a high aspect ratio.[1] As efficient swimming greatly benefits fish growth and productivity, the pursuit of high efficiency is one of the evolutionarily optimal parameters for the fish caudal fin. Optimal morphologies for periodic body/caudal fin (BCF) propulsions were previously identified from previous hydromechanical theories and verified experimentally.[2–4] It was proposed that the typical body shapes of tunas and their relatives were the optimal morphology since a high-aspect-ratio crescent-shape caudal fin could increase thrust and a narrow caudal peduncle in front of the caudal fin could reduce power consumption.[3–7] Comparison with a rectangular tail showed that a curved leading edge, as in lunate tails, resulted in a reduced thrust contribution from the leading edge suction for the same total thrust.[8] When studying the idealized heaving and pitching motion of plates with three different shapes, Li et al. showed that the tuna-tail-like forked plate was efficient, while a mildly forked plate (similar to the carp caudal fin) generated large thrust.[9] Van Buren used the digital particle velocimetry (DPIV) technique to quantify the flow field and found that as the trailing edge shape changed from convex to concave, the efficiency as well as the thrust decreased significantly.[10] Feilich et al. used a mechanically-actuated flapping foil model to study how the shape and caudal peduncle depth affect different aspects of swimming performance. They found that there was no single

[1]School of Mechanical Engineering, Dongguan University of Technology, Dongguan, China
[2]Shien-Ming Wu School of Intelligent Engineering, South China University of Technology, Guangzhou, China
[3]Division of Mechanics, Beijing Computational Science Research Center, Beijing, China

Corresponding author:
Yang Ding, Division of Mechanics, Beijing Computational Science Research Center, Beijing 100193, China.
Email: dingyang@csrc.ac.cn

optimal foil exhibiting the highest performance in all metrics.[11]

All the aforementioned studies utilized simplified isolated caudal fins and ignored the interaction between the body and the caudal fin. Since the flow incident on the caudal fin is in large part determined by the movement of the body in front of it, an isolated caudal fin without a body component may not accurately model caudal fin hydrodynamics in freely swimming fish. Borazjani et al. reconstructed a fish swimming model by including both the body and caudal fin to investigate the effect of body form and kinematics on the fluid dynamics of undulatory swimming.[12] They revealed that no combination of undulatory forms (carangiform and anguilliform) and body forms (mackerel and lamprey) achieves the highest speed or highest efficiency in all flow regions (viscous to inertial). Matta et al. tethered the robotic tuna in a circulating water tunnel and studied the performance of rectangular, elliptical and back-swept caudal fins with same area and aspect ratio. They found that the swept fin generated greatest thrust and best stabilised the leading edge vortex on the caudal fin. Liu et al. further included median fins as well as the body in the model and discovered that the body-fin and fin-fin interactions enhance thrust production in swimming.[13,14]

In this paper, we aim to create a fish model with both the body and caudal fin to investigate the effect of the tail shape on the hydrodynamics of undulatory swimming. Utilizing a self-propelled fish model with the same body shape and undulatory kinematics, we study three typical geometries of caudal fins: round, indented and lunate shape, which correspond to the tails of snakehead fish (*Channidae*), saithe (*Pollachius virens*) and tuna (*Thunnus thynnus*), respectively.

Materials and methods

Kinematics reconstruction

The morphology of the fish model used in this study originates from a fish-like autonomous underwater vehicle (AUV) designed in a laboratory[15] (Figure 1(a)). This fish-like AUV utilizes a streamlined body shape (NACA0012 from the top view) and is propelled by a novel wire-driven approach. It possesses high performance in terms of cruising speed and efficiency compared with other fish-like robots.[16–19] The pectoral fin pair in the robot fish used to control the body pitch is trimmed out, as it is usually closely pressed against the body of real fish.[20] Only the body and caudal fin are included in the model in this study (Figure 1(b)). In order to study the performance of different caudal fin shapes for the aforementioned robot fish optimization and target solely on the fluid dynamic basis of caudal fins, the shape of the body is the same for the three swimmers in this study, but different caudal fins are used: I) a round one corresponding to snakehead fish (*Channidae*); II) an indented one corresponding to saithe (*Pollachius*

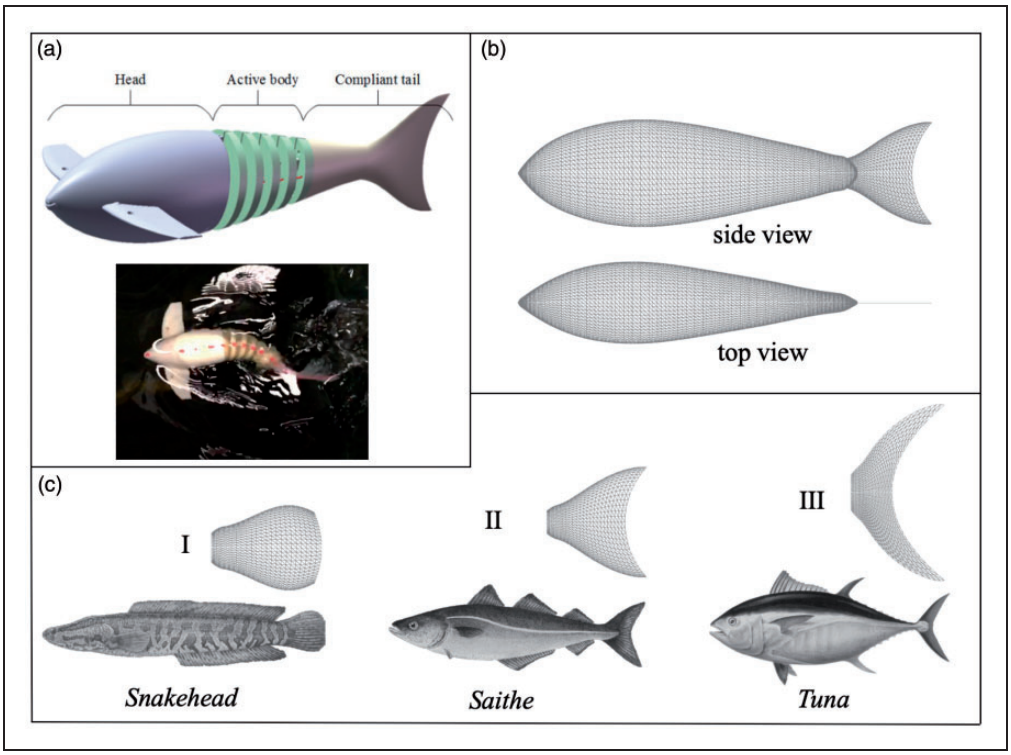

Figure 1. Illustration of the fish-like AUV and the geometry created based on it. (a) Fish-like AUV component illustration and its swimming behavior in water.[15] (b) The lateral view and top view of the model. (c) Three different caudal fins and their corresponding fish species.

virens); and III) a lunate one corresponding to tuna (*Thunnus thynnus*) (Figure 1(c)). These fins are of the same surface area $S = 0.271$ and same length $l_c = 0.209$, but of different values on height h_c, aspect ratio $AR = h_c^2/S$, first moment of the area $\hat{r_1} = \int r dS/S$, and second moment of the area $\hat{r_2}^2 = \int r^2 dS/S$ (r is the distance from the peduncle) (Figure 1(c) and Table 1).

The prespecified kinematics for the body/caudal fin follows the model of Borazjani et al.,[12] which is in the form of a backward traveling wave, with the wave amplitude varying from the head to the tail of the fish:

$$h(l,t) = a(l)\sin(kl - \omega t) \tag{1}$$

where $h(l, t)$ is the lateral excursion of the body at time t; l is the axial direction measured from the head ($l = 0$) to the fish tail tip ($l = L$); $a(l) = a_0 + a_1 l + a_2 l^2$ is the amplitude envelope of lateral motion as a function of axial location l; k is the wave number of the body undulations $k = 2\pi/\lambda$, with λ being the wavelength; and ω is the angular frequency, with $\omega = 2\pi f$, where f is the tail beat frequency. In this study, the body length is scaled to unity, i.e., $L = 1$. The parameters are carefully determined based on the experimental data[6,12,21–23] and listed in Table 2. The amplitude of the tail tip is $A = 0.1L$.

Numerical method

A fluid solver based on a second-order accurate sharp interface immersed-boundary method is used to model the dynamics of the viscous and incompressible flow around the swimmers.[24,25] This method has been used by us to simulate the fluid dynamics of low to intermediate Reynolds number flow, such as hummingbird flight[26,27] and fish swimming.[28,29] The method employs a multi-dimensional ghost-cell methodology to satisfy the boundary conditions on the immersed boundary and it is a method for addressing fluid dynamics problems with largely displaced moving boundaries.[18,19] The complex immersed body surfaces are represented by grids consisting of unstructured triangular elements and the flow is computed with the non-uniform Cartesian grids. In addition, this numerical method has also been successfully used by other researchers to investigate the hydrodynamics of fish swimming.[14,30] The governing equations of the flow are:

$$\nabla \cdot \mathbf{u} = 0 \tag{2}$$

$$\frac{\partial \mathbf{u}}{\partial t} + (\mathbf{u} \cdot \nabla)\mathbf{u} = -\frac{1}{\rho}\nabla p + \nu \Delta \mathbf{u} \tag{3}$$

where $\mathbf{u}$ denotes the velocity vector and ρ and ν are the density and kinematic viscosity of water, respectively. The non-uniform Cartesian grid covers the entire computational domain, including both the fluid region and the solid body. A standard second-order central difference scheme is used to discretize all the spatial derivatives at the nodes located in the bulk flow region. The incompressible momentum equation is integrated in time using a variation of Chorin's projection method which consists of three sub-steps. In the first sub-step, an advection–diffusion equation is solved in the absence of the pressure, and an intermediate velocity field, u_i^*, is obtained. In this step, both the nonlinear advection terms and the viscous terms are discretized using the Crank–Nicolson scheme to improve the numerical stability. The discrete equation is written as

$$\frac{u_i^* - u_i^n}{\Delta t} + \frac{1}{2}\left[\frac{\delta(U_j u_i)^*}{\delta x_j} + \frac{\delta(U_j u_i)^n}{\delta x_j}\right] = \frac{\nu}{2}\left[\frac{\delta}{\delta x_j}\left(\frac{\delta u_i^*}{\delta x_j}\right) + \frac{\delta}{\delta x_j}\left(\frac{\delta u_i^n}{\delta x_j}\right)\right] \tag{4}$$

where U_j is the velocity discretized at the face center of a computational cell, and $\frac{\delta}{\delta x_j}$ represents a finite-difference approximation of the spatial derivative using a second-order central scheme. The three components of the face-centered velocity, U_j, is obtained by computing the linear average of u_j along the j-direction. The nonlinear algebraic system is solved by a successive substitution approach. That is, the system (4) is first linearized with U_j^* computed from available u_i^* and held constant, and then the entire linear system is iterated for once using the Gauss–Seidel method before U_j^* is updated for the next iteration.

In the second sub-step, a projection function is solved as an approximation of the pressure,

$$\frac{\delta}{\delta x_j}\left(\frac{\delta p^{n+1}}{\delta x_j}\right) = \frac{\rho}{\Delta t}\frac{\delta U_j^*}{\delta x_j} \tag{5}$$

and an inhomogeneous Neumann boundary condition is imposed at all boundaries. The Poisson

Table 1. The geometrical parameters of the three caudal fins considered in this study.

Tail type	S	l_c	h_c	AR	$\hat{r_1}$	$\hat{r_2}^2$
Round	0.0271	0.209	0.161	0.96	0.122	0.0182
Indented	0.0271	0.209	0.231	1.97	0.116	0.0161
Lunate	0.0271	0.209	0.375	5.19	0.085	0.0092

Table 2. Parameters that define the traveling wave of the swimmer middle line.

Parameter	a_0	a_1	a_2	a_{max}	ω	k	λ
Value	0.02	−0.08	0.16	0.1	6π	2.1π	0.95

equation (5) is solved with a multi-grid solver. Once the pressure is obtained, the cell-centered velocity is updated as

$$u_i^{n+1} = u_i^* - \frac{\Delta t}{\rho}\frac{\delta p^{n+1}}{\delta x_i} \tag{6}$$

and the final face-centered velocity, U_i^{n+1}, is updated by averaging u_i^{n+1} along the j-direction.

The fluid-solid interface is represented by a set of Lagrangian marker points and 3-node triangular elements. To implement the boundary conditions at the interface, "ghost nodes" outside the fluid region are defined at each time step, at which the flow variables are extrapolated.[24,31] To suppress the numerical oscillations that may happen when solving a moving-boundary problem, "hybrid nodes" are defined inside the fluid region, at which the flow variables are weighted averages between the interpolated solution and the solution to the Navier–Stokes equations.

After the flow field is solved, the force exerting on the swimmer is computed by integrating the pressure and shear stress with

$$\mathbf{F} = -\int_{\partial B} (-p\mathbf{n} + \boldsymbol{\tau}) dS \tag{7}$$

where ∂B is the entire surface, $\mathbf{n}$ is the unit normal vector of surface pointing out of the fluid volume, and $\boldsymbol{\tau}$ is the shear stress acting on the surface.

In this study, the fluid-body interaction is included by implementing the loose coupling (LC-FSI) explicit projection method.[12] The translational motion of each swimmer's center of mass is obtained by solving the equation of Newton's second law of motion:

$$M\frac{d\mathbf{U}}{dt} = \mathbf{F} \tag{8}$$

$$\frac{d\mathbf{r}}{dt} = \mathbf{U} \tag{9}$$

where M is the mass of the swimmer, $\mathbf{U}$ is the velocity vector of the center of mass (CoM), $\mathbf{F}$ is the integrative force vector and $\mathbf{r}$ is the displacement of CoM of the swimmer. As the absence of the dorsal and anal fins in current model might exaggerate the rotation of the swimmer,[32,33] and introduction of rotation also cause the non-unidirectional motion, the rotation kinematics of the swimmer is constrained in this study. The Eq. 8 and 9 are solved using the second order Runge-Kutta method to maintain the overall second-order accuracy of the solver.

The Courant-Friedrichs-Lewy (CFL) condition is less than 0.5 in the entire domain throughout the simulation. The fluid solver was validated for flapping-wing simulations against both experimental and simulation data.[34] Aside from the validations of the algorithm on a more complex geometry, such as hummingbird flapping against an experimental measurement.[26,27] we further ran the self-propelled swimming and compare the cruising speed as well as the non-dimensional side power $C_p^0 = P/\rho U_0^3 L^2$, using the same geometry and kinematics of mackerel fish from Borazjani & Sotiropoulos's paper.[12] The scaled average velocity $U^* = U/U_\circ$ in the present study is 1.01, which is similar to 0.98 in Borazjani & Sotiropoulos's paper with a difference of 3.2%.[12] Regarding to the non-dimensional side power C_p^0, the comparison of in cruising swimming against Borazjani & Sotiropoulos's plot is shown in Figure 2(b).

Simulation setup

A triangular unstructured mesh is utilized to represent the fish surface, with the body having 4920 node points and 9840 elements and the tail having 713 node points and 1320 elements. The computational domain is discretized by a static nonuniform Cartesian grid. The entire domain size is $7L \times 5L \times 4L$, which is large enough to obtain converged results based on test simulations with different domain sizes. The grid is the finest in the region around the fish model, with the resolution in each dimension $\Delta = 1/150$, and this region size is $1.6L \times 0.6L \times 0.6L$; the grid is stretched to a relatively low resolution in the region far away from the model with a stretching ratio less than 1.2 (Figure 3). The total number of grids in the computational domain is 10.2 million. A frame of the computational domain is also shown in Figure 3, with X, Y and Z denoting the streamwise, lateral and vertical directions, respectively. The inlet on the left is set as the constant velocity boundary condition; the outlet on the right is set as the zero gradient boundary condition for both the velocity and pressure; and other boundaries are set as zero-stress boundary conditions to approximate infinitely far boundaries. The fish model surface is set under the no-slip and no-penetration boundary conditions. Two other resolutions in the fine mesh region are used for the mesh convergence study: 1) a coarse mesh: $\Delta = 1/120$; 2) a

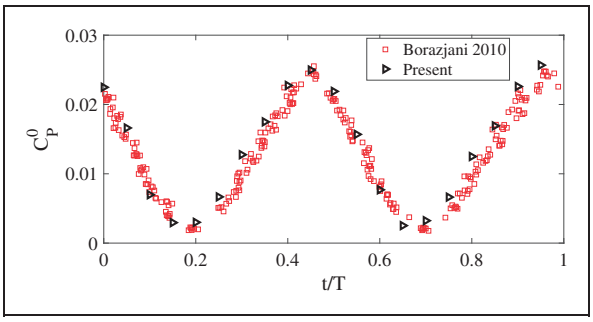

Figure 2. The validation of the non-dimensional side power C_p^0 with Borazjani & Sotiropoulos's data (Figure 6(b) in reference[12]) C_p^0 of seven cycles were digitized and then put together (red square). The present data (black triange) is from the last cycle when the cycle average speed became steady.

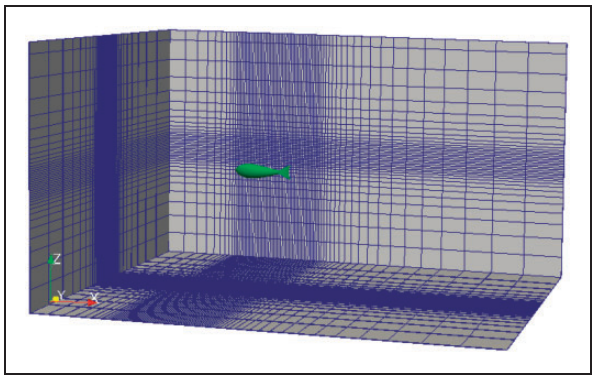

Figure 3. The simulation configuration and the nonuniform Cartesian grid distribution in the computational domain.

Table 3. The average equilibrium speed and thrust variation under three different mesh resolutions. $\bar{V}_X$ is the average cruising speed, $\bar{C}_X$ is the average thrust coefficient on the tail, $\delta\bar{V}_X$ and $\delta\bar{C}_X$ are the difference percentages with respect to values in the baseline case.

Parameter	$\bar{V}_X$	$\delta\bar{V}_X$	$\bar{C}_X$	$\delta\bar{C}_X$
Baseline	1.428	–	0.291	–
Coarse	1.434	0.42%	0.283	2.7%
Fine	1.424	0.28%	0.298	2.4%

fine mesh: $\Delta = 1/200$. For the freely swimming case, both final equilibrium speeds differ by only less than 0.5% from the baseline simulation on both the coarse and fine mesh; by contrast, the difference in average nondimensional thrusts produced by the tail is less than 3.0% (Table 3 and Figure 4). In this study, the Reynolds number is defined by the tail flapping velocity: $Re_i = 4fAL/\nu \sim 4000$. The Strouhal number $St = Uf/A$ in this study cannot be prespecified initially due to the unknown final coasting speed U. MPI parallel computing with 48 cores is adopted.

In the self-propelled model, the swimmers should travel over a long distance to reach a status equivalent to the static one, which requires a long and fine resolution in the streamwise dimension. To shorten the fine resolution length in the streamwise direction, a nonzero velocity close to the final equilibrium speed is set at the inlet: $U_i = 1.3L/s$. The velocity over time is shown in Figure 5(a). Please note that such simulation setup can't guarantee the initial process is physically reasonable. Fortunately, when the swimmer reaches the steady coasting, the hydrodynamics is the same as swimming in a quiescent fluid flow with a simple Galilean transformation. The final coasting speed $U = U_i - U'$, and the St of the round, indented and lunate fins is 0.423, 0.420 and 0.465, respectively. Besides the forward motion, the swimmer in the simulation also exhibits a slight sideways motions. The mean lateral velocity is 0.04 L/s, which is about two orders of magnitude smaller than the forward velocity.

Efficiency

The *quasi-propulsive efficiency* η_q is utilized in this study, which represents the efficiency of the entire swimmer. η_q is defined as the ratio of the power needed to tow a body in the rigid-straight condition to the power needed for self-propulsion:[35]

$$\eta_q = \frac{D_0 U}{P_{in}} \tag{10}$$

where $D_0 = \frac{1}{2} C_{D0} \rho U^2 S_f$ is the drag experienced by a rigid-straight body with front area S_f at speed U and P_{in} is the power input over the entire body $P_{in} = \int_{S_{entire}} \mathbf{f} \cdot \mathbf{v} dS$. To obtain the drag on the rigid-straight body, a series of fixed-body simulations are run with varied incoming flow for U ranging from 1.2 to 2.1 with an interval of 0.3. The original data and the fit curve are shown in Figure 5(b). By spline interpolation, we can obtain the drag on the straight body at a certain speed U for the η_q calculation.

Results and discussions

Pressure distribution

As the caudal fin moves laterally, the stoss surface pushes away the fluid on the same side, increasing the pressure on the stoss surface of the fin. Meanwhile, the lee surface creates a 'pseudo-vacuum', forming a low-pressure region pulling the fluid nearby to fill it. We set the pressure of static fluid in the far field to zero; then, pushing fluid causes positive pressure, while pulling causes negative pressure. The first column in Figure 6 shows the pressure increase on the stoss side at $t/T = 0.20$, at which time the pressure difference across the caudal fin Δp peaks. For the round caudal fin, the fluid adjacent to the stoss surface has a strong stagnation effect under high pressure; in addition, the first moment $\hat{r}_1$ and second moment $\hat{r}_2{}^2$ of the round caudal fin are the largest, theoretically further increasing the pressure on the stoss side, as they are related to the velocity between the caudal fin and water. Therefore, p_{stoss} of the round fin is the largest among the three, while the lunate fin has the lowest pressure increase on the stoss side (Figure 6). On the lee side, the lateral movement of the fin causes a low-pressure region on the entire surface due to suction (Figure 7). Moreover, the formation of the strong leading edge vortex further decreases the pressure around the edge. As shown in the second column of Figure 6, the suction effect is strongest on the lunate fin. The pressure difference between the stoss side and lee side Δp contributes to the manifestation of propulsion. The last column in Figure 6 shows the pressure difference distribution Δp of these three caudal fins. Significant Δp is shown on

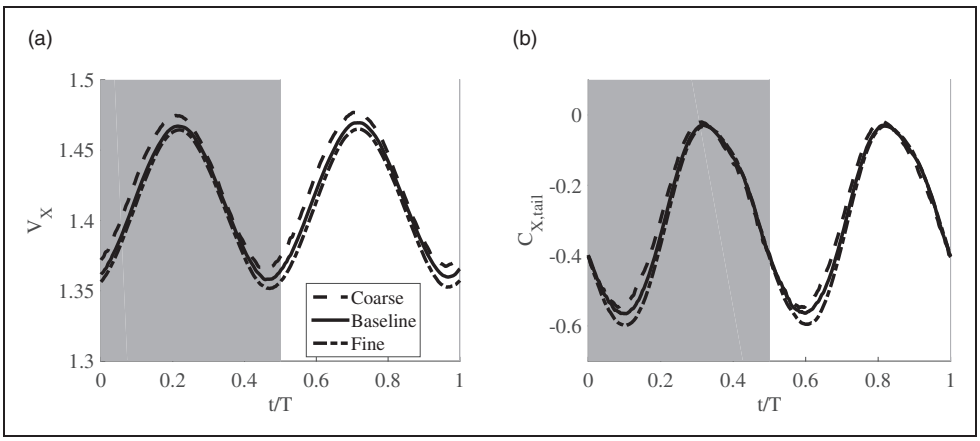

Figure 4. Mesh convergence study. A comparison of the final swimming speed V_X (a) and the caudal fin force $C_{X,tail}$ (b) at equilibrium under the three meshes.

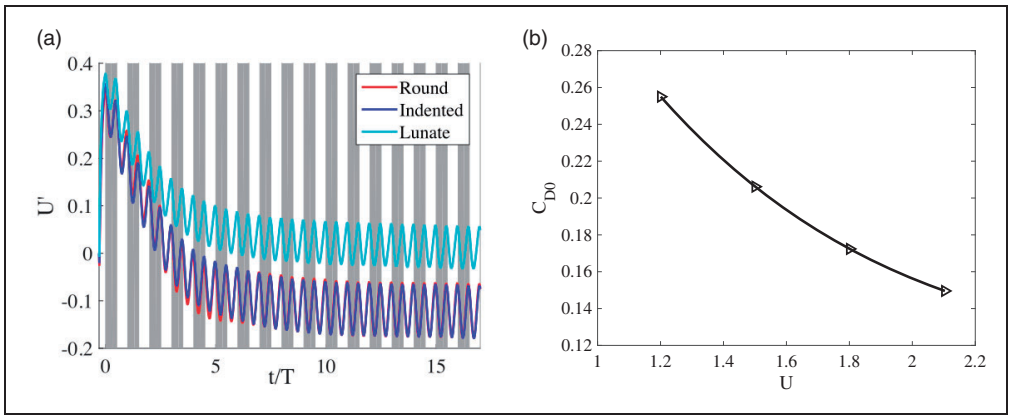

Figure 5. (a) The locomotion speed over time until equilibrium is reached for the three swimmers (the inlet velocity is set as 1.3 L/s). (b) The drag coefficient of a rigid-straight swimmer as a function of its speed.

almost the entire caudal fin except at the trailing edge for all three geometries.

Figure 8 shows the integration of the pressure difference across the caudal fin $\Delta C_p = \int_S \Delta p \mathrm{d}S/(0.5\rho U^2 S)$ and the pressure integration on its right surface C_{pr} and left surfaces C_{pl} in one cycle. In the first half-cycle, the caudal fin moves from left to right. The right side is the stoss side, and the left side is the lee side. The push-based force on the stoss side is the largest on the round fin and the weakest on the lunate fin (Figure 8(b)), while the suction-based force on the lee side is the strongest on the lunate fin and the weakest on the round fin (Figure 8(c)). In order to consolidate our findings, we introduce two complementary caudal fins with the same area but different aspect ratios (see Appendix 1). The aspect ratios of them are 1.34 and 3.39, respectively. The ΔC_p values of the five fins are of similar amplitude (Figure 8(a)), indicating similar propulsion of the swimmers. Interestingly, the intrinsic mechanism for this propulsion varies. To evaluate the significance of the pushing-based and suction-based mechanisms quantitatively, we compare the values of C_{pr} (pushing-based effect) and C_{pl} (suction-based effect) at time $t/T = 0.2$, when the propulsion is the strongest. The suction effects of these five fins with increasing AR contribute 50.8%, 55.8%, 58.1%, 67.8% and 74.2% of the pressure difference, respectively.

Aspect ratio/suction portion and efficiency

Despite the fact that the shape of the leading edge/trailing edge also affects the hydrodynamics of the caudal fin,[8] the leading edge vortex attachments on these caudal fins are similar.[36] Thus, we attribute the differences between the hydrodynamics of the caudal fins to the AR. As is shown in Figure 9(a), the suction portion of the force on the caudal fin increases with its AR. The suction is mainly caused by the presence of the leading edge vortex attached to the lee side. As the AR increases, the strength of the leading edge increases as well, thus strengthening the overall suction effect of the leading edge vortex. Figure 9(b) shows the efficiency η_q variation with the caudal fin aspect ratio. We can see that the swimming efficiency decreases with the suction portion. This is consistent with the experimental measurement on a flat plate at

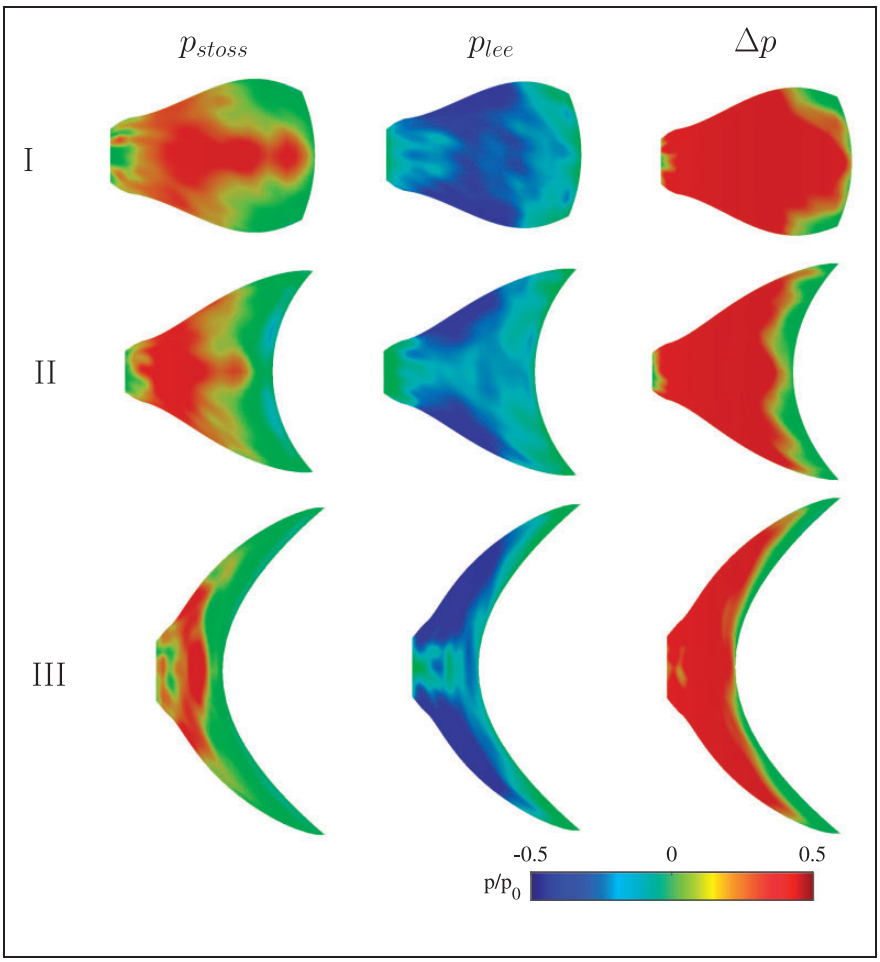

Figure 6. Pressure distribution at $t/T = 0.20$, when the pressure difference is the largest. First column: pressure on the stoss surface; second column: pressure on the lee surface; third column: the pressure difference.

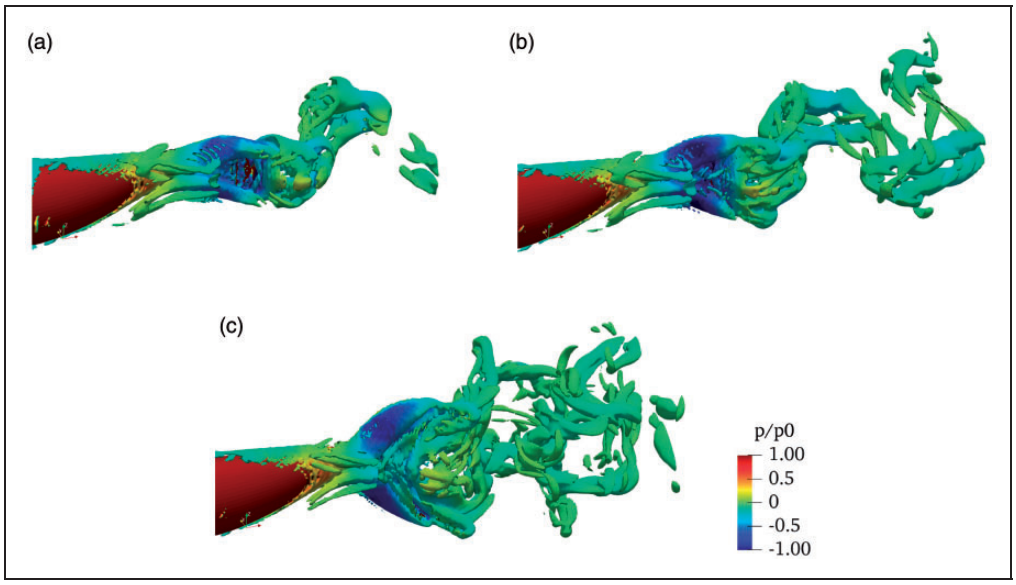

Figure 7. Vortex structure on the tail at $t/T = 0.2$ and contoured by the nondimensional pressure $p/p0$ ($p0 = 0.5\rho(2fA)^2$). (a) Round fin, (b) indented fin, and (c) lunate fin.

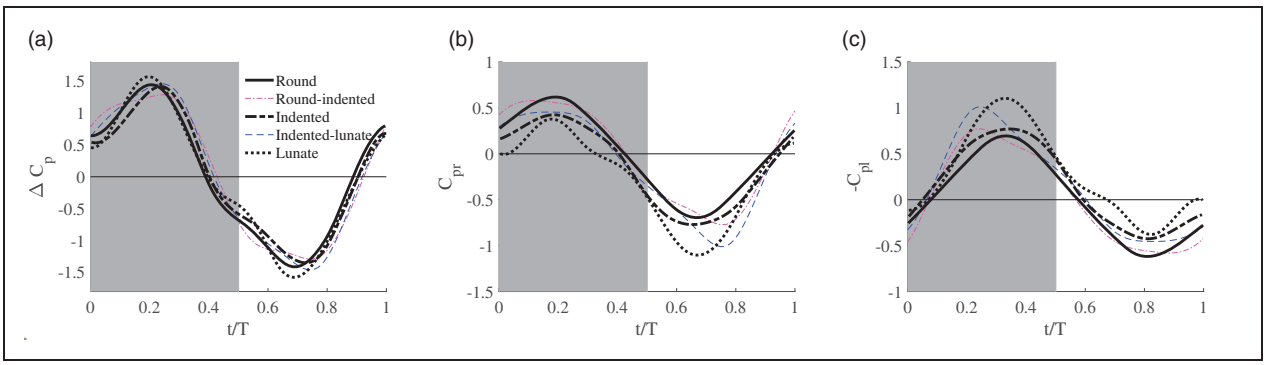

Figure 8. Time course of the pressure integration on the caudal fin of the swimmers at the baseline undulatory amplitude. (a) Pressure differences; (b) pressure on the right side of the fin; (c) flipped pressure on the left side of the fin.

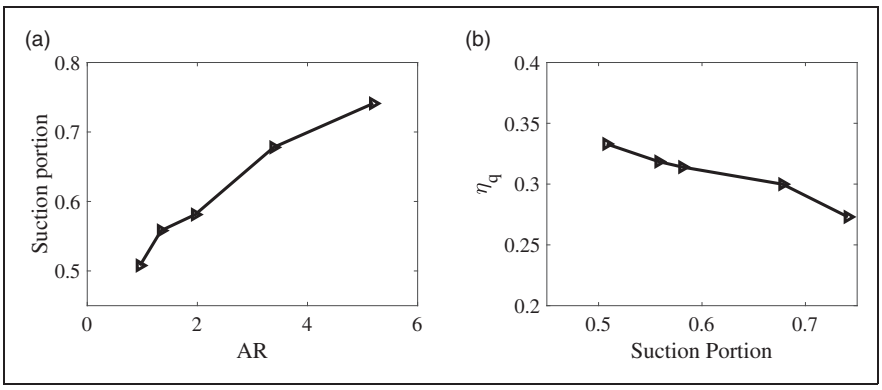

Figure 9. The correlation between the suction portion on the tail and the tail aspect ratio. (b) The swimming efficiency η_q as a function of the suction portion.

$Re = 6000$ and 10,000, which showed that a convex fin with a smaller AR is relatively more efficient.[10] By contrast, when studying the propulsion mechanism of lamprey and jellyfish, Gemmell revealed that animals could pull themselves through the water by suction, and this suction-based propulsion is more efficient than the pushing-based mechanism.[37] In the study of Gemmell et al., the propulsive mechanism of lampreys and jellyfish is altered by spinal transect, which maintains the geometry but changes the kinematics. The controlled lampreys exhibited coordinated wave-like body kinematics that traveled along the length of the animal, while the spinally transected specimens generated a standing wave of lateral body displacement.[37]

Following the same mathematical model used by Gemmell et al., the pressure on the caudal fin is decomposed into two categories: the low pressure that pulls the surface of swimmers and the high pressure that pushes the surface.[37] The "pull" and "push" effect drives the locomotion in the swimming direction X while causing resistance in the lateral direction. The efficiency is calculated using the equation:

$$\eta_{opt} = \frac{T_{X,opt}U}{T_{X,opt}U + P_{lat,opt}} \tag{11}$$

where T_X denotes the thrust, P_{lat} denotes the power consumed due to lateral movement, and the second subscript 'opt' represents a 'pull', a 'push' or their combined effect with regard to their efficiencies. Figure 10(a) shows the power coefficients variation in one cycle of the indented fin due to a 'pull', a 'push' and their combination for the indented fin case. The efficiencies of the 'pull' or 'push' effects are calculated and shown in Table 4. The push efficiency is larger than the pull efficiency for all three fins. As the AR of the caudal fin increases, the efficiency of its 'pull' and 'push' mechanism decreases. This indicates that the efficiency of the suction-based mechanism is not necessarily larger than that of the push-based one. The efficiency η in Gemmell's paper can be rewritten as

$$\eta = \frac{1}{1 + \int_S \tilde{f} \cdot \tilde{v} dS} \tag{12}$$

where the nondimensional $\tilde{f} = f_Y * S/T_X$, for which S is caudal fin area and nondimensional $\tilde{v} = v/U$, for which f_Y and v are the lateral force and velocity distributions, respectively. Here, we omit the second subscript for brevity. The efficiency is merely dependent

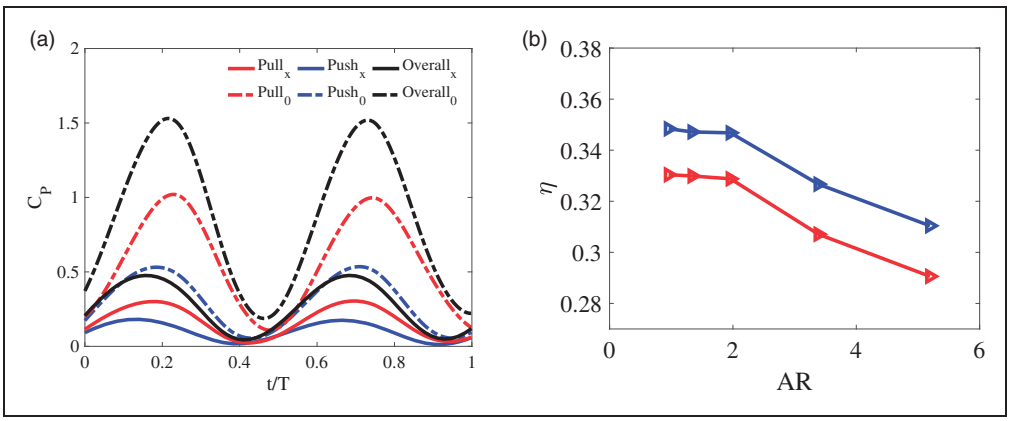

Figure 10. (a) The power coefficient variation in one cycle of tail beating. This figure shows the pull effect, the push effect and their combination. Subscript 'X' denotes the swimming direction, and subscript '0' denotes the total effect in both the swimming and lateral directions. (b) The variation in tail efficiency η under the pull and push effects for different *AR*s.

Table 4. The efficiency η of the three caudal fins as a result of the 'pull' effect, the 'push' effect and their combined effect.

Tail type	η_{Pull}	η_{Push}	$\eta_{Overall}$
Round	0.330	0.348	0.338
Indented	0.329	0.347	0.336
Lunate	0.291	0.310	0.297

on the multiplication of $\tilde{f}$ and $\tilde{v}$. From Figure 6, we can see that the 'pull' contribution is posterior to the 'push' contribution on the caudal fin. As the velocity of each location on the tail increases posterior, the multiplication of $\tilde{f}$ and $\tilde{v}$ becomes larger for the 'pull' effect, resulting in a lower efficiency η.

Flux behind the fish

As has been suggested in other studies, the muscle activity and kinematics, particularly the tail-beat amplitude and frequency control, might help in maintaining a high swimming efficiency,[38–40] which was manifested in the strength and orientation of tail vortex rings.[41] The vorticity ω_Z on the horizontal plane transecting the middle of fish is shown in Figure 11. The vortex oblique angle, which is the angle between the left shed vortex and right shed vortex, was estimated based on this ω_Z to be equal to $\theta = 34°$, $36°$, and $18°$ for round, indented and lunate caudal fins, respectively. For the 2 D foil, a large θ indicates excessive lateral momentum transferred to the flow, which contributes little to the thrust. As a result, a high vortex oblique angle θ shows the disadvantage relative to the swimming efficiency. However, because the heights of these caudal fins are different, the overall lateral momentum transferred to the flow no longer follows the 2 D prediction.

Figure 12 shows ω_X as well as the lateral velocity V_Y on this plane. The ω_X plot shows that the vortex ring of the round fin is more confined, while the lunate fin case has the widest vortex ring. Within the vortex ring, a large lateral flow is introduced. Figure 12(d) shows the lateral velocity profile of V_Y. For the round and indented fins, the peak value of V_Y is large, which indicates the large vortex angle on the middle horizontal plane. Meanwhile, the peak value of the lunate fin is only approximately half of that of the round and indented fins, which is the reason why the vortex angle of the lunate fin is the smallest. The net flux in the lateral direction of the lunate fin swimmer is the largest (0.135 L^2/s), while that of the round fin swimmer is the smallest (0.057 L^2/s). Therefore, the direct manifestation of the low efficiency of the lunate fin is the large lateral momentum flux due to the large height of the caudal fin. A similar phenomenon was observed when an elliptical plate was simulated at different Strouhal numbers (St), with a small vortex oblique angle corresponding to low efficiency.[42]

Body-fin interaction

With the presence of body before the caudal fin, the body-fin interaction is significant.[13,43] As shown in Figure 13, the vortex resulting from the posterior body (PBV) moves around the peduncle due to the pressure difference between two sides of body, and the leading edge vortex (LEV) is also generated on the anterior part of the fin. The interaction of PBV strengthens the LEV produced by the caudal fin. The characteristics is of the same pattern for all three caudal fins and similar to the finding in reference.[13] Meanwhile, the vortex shed in body boundary (BBV) due to the high curvature of the body also interact with the LEV. Since the chord length transected on this plane varies with different tail, the contribution of BBV to the LEV might change with different tail. As the leading edge vortex attributes to the suction effect, the body-fin interaction might intensify the suction-based propulsion mechanism regarding to this point. In addition, the body undulation transfers the lateral momentum to the flow and such flow

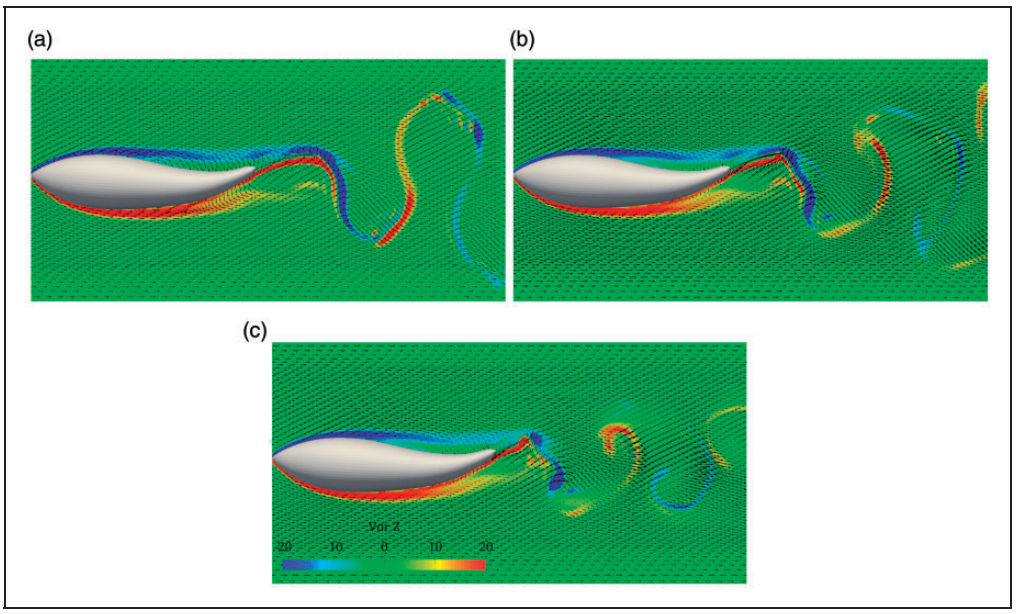

Figure 11. Flow field and ω_Z contour of the three swimmers. (a) Round fin, (b) indented fin, and (c) lunate fin.

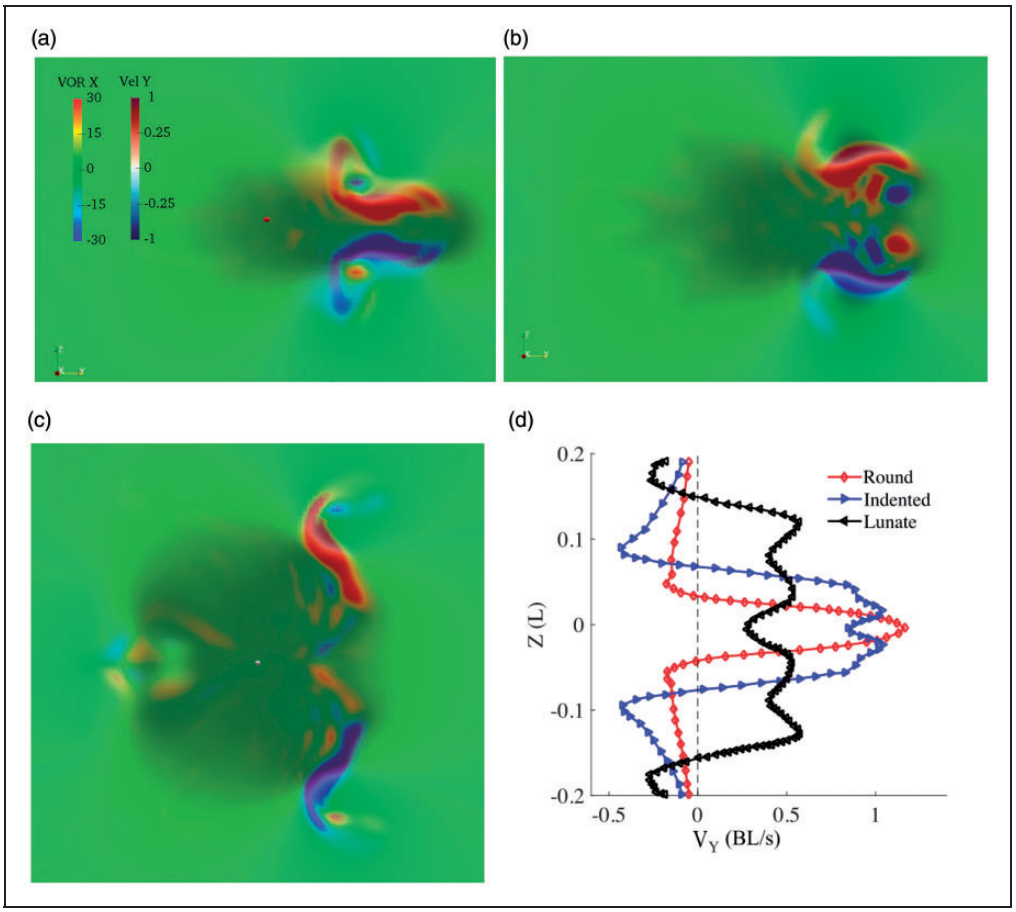

Figure 12. ω_X and the lateral velocity on the YZ plane transecting the middle of the vortex ring. a) Round fin, b) indented fin, c) lunate fin, and d) lateral velocity distribution on a straight line of a plane transecting the vortex ring vertically.

moves downward to the caudal fin.[44] Depending on the phase difference between the body and caudal fin, such lateral momentum could either increase or decrease the relative velocity between the caudal fin and flow. Regarding to the surface distribution of the caudal fin, the interaction with the lateral flow by the round caudal fin is the strongest while the lunate fin the weakest. Since all these differences of body-fin

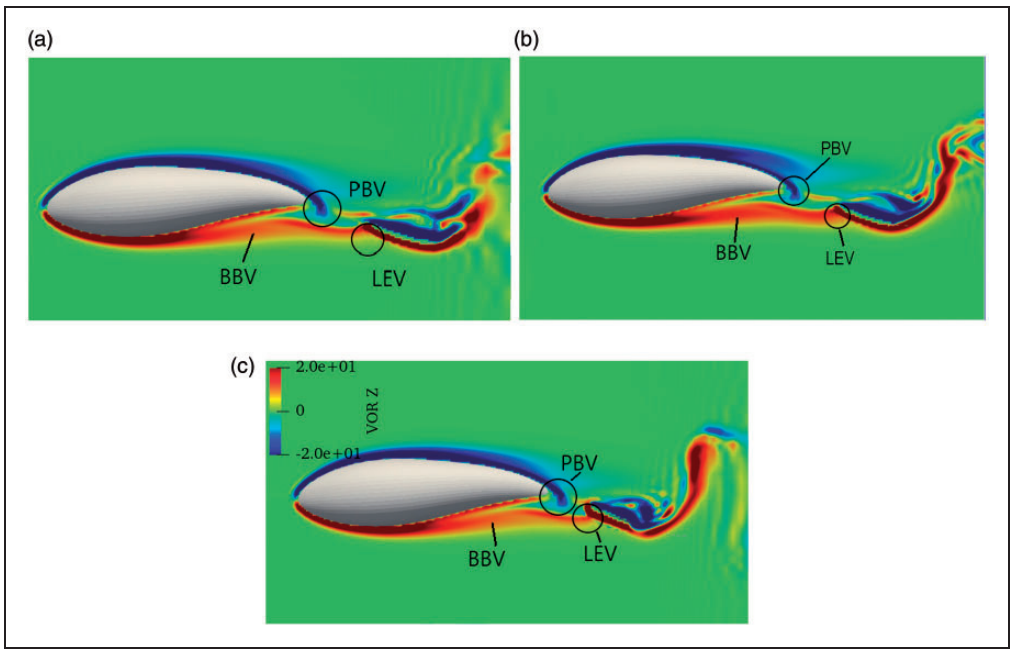

Figure 13. Wake ω_Z generated on three swimmers on the plane with 0.06L shift from the middle plane at $t/T = 0.2$. (a) Round fin, (b) indented fin, and (c) lunate fin.

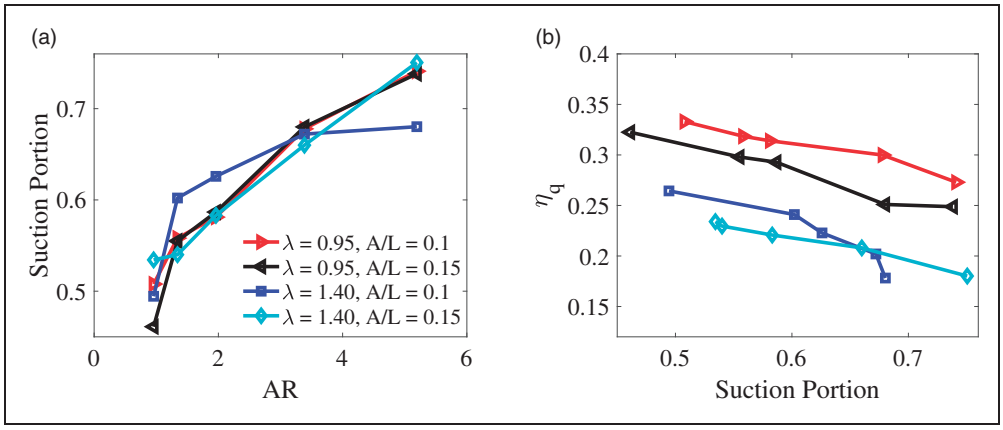

Figure 14. The correlation between the suction portion on the tail and the tail aspect ratio for different tail beat amplitudes and undulation wavelengths. (b) The swimming efficiency η_q as a function of the suction portion for different tail beat amplitudes and undulation wavelengths.

interaction originate from the shape of the caudal fin in this study, the modeling of the hydrodynamics with body and caudal have included such interactions and we didn't strip the body-fin interaction effect from other effects due to caudal fin shape.

Effect of the flapping amplitude and undulatory mode

The lateral peak-to-peak displacement at the tip of the caudal fins was approximately 0.2L and virtually independent of the swimming speed in most fish.[45] On some occasions, the tip-to-tip amplitude of the fish caudal fin ranged from 0.1L to 0.3L.[46] In this study, we also simulated the fluid dynamics of swimmers with three caudal fins for A/L = 0.15. In addition, we varied the wave number of the swimmers and simulated the kinematics with $\lambda = 1.4$ for A/L = 0.1 and A/L = 0.15. When $\lambda = 1.4$, the undulatory mode changed from the subcarangiform to thunniform, which is usually utilized by fish with high-AR tails in nature.[1] For all four kinematics settings, the suction portion and AR followed a similar trend, e.g., an increase in the AR led to a high suction portion (Figure 14(a)). All four kinematics also showed that the efficiency η_q is reversely correlated to the suction portion (Figure 14(b)). One theory shows that the leading edge suction leads to a more significant boundary-layer separation; thus, the adoption of the suction mechanism might cause a low efficiency.[8]

Limitations

Adult fish usually swim in a flow regime where *Re* ranges from 10^5 to 10^8 and inertial force dominates the flow.[46] However, we argue that the results are qualitatively representative of real adult fish despite the *Re* difference in current study. First, transition from the viscous regime to the turbulent regime of swimming fish occurs at an *Re* value of several thousands according to a meta-analysis of fish swimming data.[47] Second, the swimmers in our study show an inertia-dominated mode of swimming. In comparison, a fish with a larger *Re* will experience less drag, and their *St* numbers will be smaller and efficiency will be higher as well. In addition, the model in this study includes only the body and caudal fin while excluding the dorsal/anal fins. A previous study has shown high-performance propulsion by utilizing complex interactions among the dorsal, anal, and caudal fins and the body.[13] Hence, the inclusion of the dorsal/anal fins might lead to slightly higher efficiency than that presented in the current study. Because these fins have ancillary roles, their hydrodynamic effect is beyond the scope of this paper.

Conclusions

In this paper, we utilize a self-propelled fish model to study the hydrodynamics of swimmers with three caudal fin shapes: round, indented and lunate. The simulation results show that their propulsion mechanisms are different: the low-aspect-ratio round fin uses a combined pushing/suction propulsive mechanism; the high-aspect-ratio lunate fin uses a suction-dominated propulsive mechanism; and the indented fin, the aspect ratio of which is between those of the previous two, uses a propulsive mechanism that is also representative of a middle ground between the previous two. Contrary to the findings from previous studies on lamprey and jellyfish, the suction-based mechanism is not prone to high efficiency; in fact, the most suction-based mechanism leads to the lowest efficiency and the least suction-based mechanism lead to the highest efficiency.

Declaration of Conflicting Interests

The author(s) declared no potential conflicts of interest with respect to the research, authorship, and/or publication of this article.

Funding

The author(s) disclosed receipt of the following financial support for the research, authorship, and/or publication of this article: This project was partially funded by the National Key Research and Development Program of China (2017YFB1300203) and the Key Laboratory of Robotics and Intelligent Equipment of Guangdong Regular Institutions of Higher Education (Grant No.2017KSYS009) to L. Yin and J. Song; the Strategic Priority Research Program of the Chinese Academy of Sciences (class A) (Grant No. XDA22040203) and the Fundamental Research Funds for the Central Universities (Grant No. 2019XX01) to Y. Zhong; and an NSFC grant No. 11672029 and NSAF-NSFC grant No. U1930402 to Y. Ding.

ORCID iD

Yang Ding https://orcid.org/0000-0002-8252-2421

References

1. Lindsey CC. Form, function, and locomotory habits in fish. *Fish Physiol* 1979; 7: 1–100.
2. Lighthill MJ. Hydromechanics of aquatic animal propulsion. *Annu Rev Fluid Mech* 1969; 1: 413–446.
3. Lighthill MJ. Aquatic animal propulsion of high hydromechanical efficiency. *J Fluid Mech* 1970; 44: 265–301.
4. Blake RW, Li J and Chan KHS. Swimming in four goldfish *Carassius auratus* morphotypes: understanding functional design and performance employing artificially selected forms. *J Fish Biol* 2009; 75: 591–617.
5. Webb PW. Body form, locomotion and foraging in aquatic vertebrates. *Am Zool* 1984; 24: 107–120.
6. Webb PW. Steady' swimming kinematics of tiger musky, an esociform accelerator, and rainbow trout, a generalist cruiser. *J Exp Biol* 1988; 138: 51–69.
7. Wolfgang MJ, Anderson JM, Grosenbaugh MA, et al. Near-body flow dynamics in swimming fish. *J Exp Biol* 1999; 202: 2303–2327.
8. Chopra MG and Kambe T. Hydromechanics of lunate-tail swimming propulsion. Part 2. *J Fluid Mech* 1977; 79: 49–69.
9. Li G-j, Zhu L and Lu X-y. Numerical studies on locomotion perfromance of fish-like tail fins. *J Hydrodyn* 2012; 24: 488–495.
10. Van Buren T, Floryan D, Brunner D, et al. Impact of trailing edge shape on the wake and propulsive performance of pitching panels. *Phys Rev Fluids* 2017; 2: 014702.
11. Feilich KL and Lauder GV. Passive mechanical models of fish caudal fins: effects of shape and stiffness on self-propulsion. *Bioinspiration Biomim* 2015; 10: 036002.
12. Borazjani I and Sotiropoulos F. On the role of form and kinematics on the hydrodynamics of self-propelled body/caudal fin swimming. *J Exp Biol* 2010; 213: 89–107.
13. Liu G, Ren Y, Dong H, et al. Computational analysis of vortex dynamics and performance enhancement due to body–fin and fin–fin interactions in fish-like locomotion. *J Fluid Mech* 2017; 829: 65–88.
14. Han P, George V, Lauder H, et al. Hydrodynamics of median-fin interactions in fish-like locomotion: effects of fin shape and movement. *Phys Fluids* 2020; 32: 011902.

15. Zhong Y and Du R. Parametric study of the swimming performance of a novel robot fish with active compliant propulsion mechanism. In: *Proceedings of the ASME 2016 International Design Engineering Technical Conferences and Computers and Information in Engineering Conference, Volume 5A: 40th Mechanisms and Robotics Conference,* Charlotte, North Carolina, USA, 21-24 August, 2016.
16. Liu J, Dukes I and Hu H. Novel mechatronics design for a robotic fish. In: *2005 IEEE/RSJ International Conference on Intelligent Robots and Systems*, Edmonton, Alta., 2005, pp. 807–812. IEEE.
17. Valdivia y Alvarado P and Youcef-Toumi K. Design of machines with compliant bodies for biomimetic locomotion in liquid environments. *J Dyn Syst, Meas, Control* 2006; 128: 3–13.
18. Epps BP, Valdivia y Alvarado P, Youcef-Toumi K, et al. Swimming performance of a biomimetic compliant fish-like robot. *Exp Fluids* 2009; 47: 927–939.
19. Liu J-D and Hu H. Biologically inspired behaviour design for autonomous robotic fish. *Int J Automat Comput* 2006; 3: 336–347.
20. Bainbridge R. Caudal fin and body movement in the propulsion of some fish. *J Exp Biol* 1963; 40: 23–56.
21. Bainbridge R. The speed of swimming of fish as related to size and to the frequency and amplitude of the tail beat. *J Exp Biol* 1958; 35: 109–133.
22. Liao JC. The role of the lateral line and vision on body kinematics and hydrodynamic preference of rainbow trout in turbulent flow. *J Exp Biol* 2006; 209: 4077–4090.
23. Jayne BC and Lauder GV. Speed effects on midline kinematics during steady undulatory swimming of largemouth bass, *Micropterus salmoides*. *J Exp Biol* 1995; 198: 585–602.
24. Luo H, Dai H, de Sousa PF, et al. On the numerical oscillation of the direct-forcing immersed-boundary method for moving boundaries. *Comput Fluids* 2012; 56: 61–76.
25. Tian F, Dai H, Luo H, et al. Fluid-structure interaction involving large deformations: 3d simulations and applications to biological systems. *J Comput Phys* 2014; 258: 451–469.
26. Song J, Luo H and Hedrick TL. Three-dimensional flow and lift characteristics of a hovering ruby-throated hummingbird. *J R Soc Interface* 2014; 11: 20140541.
27. Song J, Tobalske BW, Powers DR, et al. Three-dimensional simulation for fast forward flight of a calliope hummingbird. *R Soc Open Sci* 2016; 3: 160230.
28. Song J, Zhong Y, Luo H, et al. Hydrodynamics of larval fish quick turning: a computational study. *Proc IMechE, Part C: J Mechanical Engineering Science* 2018; 232: 2515–2523.
29. Ming T, Jin B, Song J, et al. 3d computational models explain muscle activation patterns and energetic functions of internal structures in fish swimming. *PLOS Comput Biol* 2019; 15: e1006883.
30. Wang J, Wainwright DK, Lindengren RE, et al. Tuna locomotion: a computational hydrodynamic analysis of finlet function. *J R Soc Interface* 2020; 17: 20190590.
31. Mittal R, Dong H, Bozkurttas M, et al. A versatile sharp interface immersed boundary method for incompressible flows with complex boundaries. *J Comput Phys* 2008; 227: 4825–4852.
32. Blake RW. Fish functional design and swimming performance. *J Fish Biol* 2004; 65: 1193–1222.
33. Maia A, Lauder GV and Wilga CD. Hydrodynamic function of dorsal fins in spiny dogfish and bamboo sharks during steady swimming. *J Exp Biol* 2017; 220: 3967–3975.
34. Dai H, Luo H and Doyle JF. Dynamic pitching of an elastic rectangular wing in hovering motion. *J Fluid Mech* 2012; 693: 473–499.
35. Triantafyllou MS, Yue DKP and Maertens AP. Efficiency of fish propulsion. *Bioinspir Biomimet* 2015; 10: 046013–046023.
36. Borazjani I and Daghooghi M. The fish tail motion forms an attached leading edge vortex. *Proc R Soc B* 2013; 280: 20122071.
37. Gemmell BJ, Colin SP, Costello JH, et al. Suction-based propulsion as a basis for efficient animal swimming. *Nat Commun* 2015; 6: 8790.
38. Eloy C. On the best design for undulatory swimming. *J Fluid Mech* 2013; 717: 48–89.
39. Van Rees WM, Gazzola M and Koumoutsakos P. Optimal morphokinematics for undulatory swimmers at intermediate Reynolds numbers. *J Fluid Mech* 2015; 775: 178–188.
40. Anderson JM, Streitlien K, Barrett DS, et al. Oscillating foils of high propulsive efficiency. *J Fluid Mech* 1998; 360: 41–72.
41. Akanyeti O, Putney J, Yanagitsuru YR, et al. Accelerating fishes increase propulsive efficiency by modulating vortex ring geometry. *Proc Natl Acad Sci USA* 2017; 114: 13828–13833.
42. Li C and Dong H. Three-dimensional wake topology and propulsive performance of low-aspect-ratio pitching-rolling plates. *Phys Fluids* 2016; 28: 071901.
43. Brooks S and Green MA. Experimental study of body-fin interaction and vortex dynamics generated by a two degree-of-freedom fish model. *Biomimetics* 2019; 4: 67.
44. Standen EM and Lauder GV. Hydrodynamic function of dorsal and anal fins in brook trout(*Salvelinus fontinalis*). *J Exp Biol* 2007; 210: 325–339.
45. Shadwick RE and Lauder GV. *Fish physiology: Fish biomechanics*. 1st Ed. 2006. Academic Press.
46. Biewener A and Patek S. *Animal locomotion*. Oxford: Oxford University Press, 2018.
47. J, Fransje van Weerden DAP, Reid CK and Hemelrijk A. Meta-analysis of steady undulatory swimming. *Fish Fish* 2014; 15: 397–409.

Appendix 1. Complementary caudal fins

As three caudal fins might provide faulty correlation between AR, suction-based ratio and efficiency, two complementary caudal fins are introduced to the

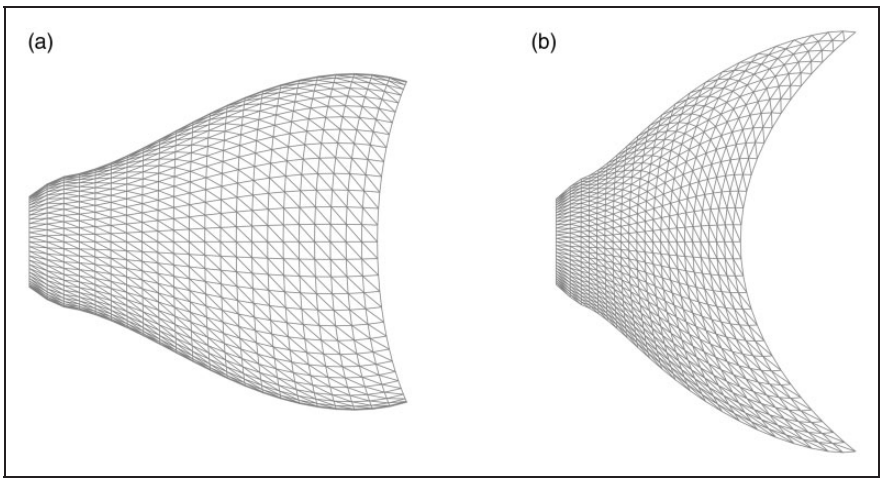

Figure 15. Two complementary caudal fins for a more rigorous relation between AR, suction-based ratio and efficiency. (a) Average geometry between the round and indented caudal fins; (b) Average geometry between the indented and lunate caudal fins.

simulations. These two caudal fins are not selected based on any prototype deliberately, but built according to the existing three fins. One is the average geometry between the round and indented caudal fins ($AR = 1.34$) (Figure 15(a)); and the other one is the average geometry between the indented and lunate caudal fins ($AR = 3.39$)(Figure 15(b)). The height of caudal fin h_c is adjusted to maintain the same area.